Materials Advances

ROYAL SOCIETY OF CHEMISTRY

PAPER

View Article Online
View Journal | View Issue

Open Access Article. Published on 28 October 2025. Downloaded on 2/12/2026 8:07:39 AM.
This article is licensed under a Creative Commons Attribution 3.0 Unported Licence.

Check for updates

Cite this: *Mater. Adv.*, 2025, **6**, 9746

Negative thermal quenching and optically stable Tb^{3+}-doped tungstate phosphor for high temperature lighting and advanced thermometry applications

R. Kiran,[a] S. Masilla Moses Kennedy,[b] A. Princy,[b] M. I. Sayyed,[cd]
Aljawhara H. Almuqrin[e] and Sudha D. Kamath *[a]

Received 19th June 2025,
Accepted 26th October 2025

DOI: 10.1039/d5ma00655d

rsc.li/materials-advances

This study reports the anomalous temperature-dependent luminescence behaviour of Tb^{3+}-doped Ca_2MgWO_6 double perovskite phosphors designed for multifunctional optical and temperature sensing applications. The optimized composition (6 mol% Tb^{3+}) results in an unusual enhancement (∼242%) of the green emission intensity ($^5D_4 \rightarrow {}^7F_5$, 546 nm) with increasing temperature, which indicates negative thermal quenching. This phenomenon is attributed to the thermally stimulated carrier release from the $Tb_{Ca} + V''_{Ca} + V_O$ defect complexes and their subsequent recombination at the luminescent centers. The optimized phosphor demonstrates excellent thermal stability and consistent luminescent performance in the green spectral region. Diffused reflectance revealed a direct band gap of approximately 3.24 eV and a refractive index near 2.33, supporting its wide-band-gap semiconducting nature. Fluorescence intensity ratio-based thermometric evaluation yields a maximum absolute and relative sensitivity of 1.46×10^{-4} K^{-1} and 0.05% K^{-1}, respectively, highlighting its potential for efficient high-temperature optical sensing and lighting applications.

1. Introduction

Rare earth (RE)-doped phosphors have emerged as a vital class of functional materials in modern materials science owing to their luminescence properties and structural stability.[1,2] The strategic incorporation of one or more RE or transition metal ions into the host lattice has enabled the development of phosphors with sharp emission, enhanced emission efficiency, thermal stability, and colour tunability.[3–5] These attributes make them indispensable in a broad spectrum of advanced applications, including high-performance light-emitting diodes (LEDs), sensitive and selective luminescent sensors for environmental and biological monitoring, and next-generation energy solutions, like solar concentrators and persistent luminescence-based energy storage systems.[6–14]

Among the various applications, phosphor-based fluorescence thermometry is a promising technique owing to its non-contact nature, miniaturization, rapid response, and high temperature sensitivity. In this technique, temperature sensing can be achieved through the fluorescence intensity, spectral shift, bandwidth, lifetime, or fluorescence intensity ratio (FIR). Among these, FIR-based and lifetime-based methods are preferred owing to their self-referencing capability, which minimizes errors from excitation or detection fluctuations.[15] However, the FIR is more susceptible to light source instability and measurement variations. In contrast, fluorescence lifetime thermometry offers higher precision by extracting thermal information from decay curves that are independent of external influences. Since fluorescence lifetime signals occur over nanosecond to millisecond timescales, this method ensures excellent sensitivity, electromagnetic immunity, and self-correction capability, making it ideal for accurate temperature monitoring.[16,17] Several phosphors have been previously investigated for temperature sensing, including $Ca_2Al_2SiO_7$:Tb^{3+}, K^+,[18] $Y_2Mg_2Al_2Si_2O_{12}$:Bi^{3+}, Eu^{3+},[19] $Li_2Ba_5W_3O_{15}$:Pr^{3+},[20] $La_2Ti_2O_7$:Yb^{3+}, Er^{3+},[21] $Sr_3TaGa_3Si_2O_{14}$:Tb^{3+}, Eu^{3+},[22] Ba_2LaNbO_6:Mn^{4+},[23] $Li_2Ba_5W_3O_{15}$:Dy^{3+},[24] Gd_2GaSbO_7:Bi^{3+}, Eu^{3+},[25] $BaGa_{12}O_{19}$:Cr^{3+}, Mn^{2+}[26] and $Y_7O_6F_9$:Eu^{3+}.[27]

---

[a] Department of Physics, Manipal Institute of Technology, Manipal Academy of Higher Education, Manipal, Karnataka, India. E-mail: sudha.kamath@manipal.edu
[b] Sri Siva Subramaniya Nadar College of Engineering, Tamil Nadu, India
[c] Department of Physics, Dogus University, Dudullu-Ümraniye, 34775 Istanbul, Türkiye
[d] Department of Physics and Technical Sciences, Western Caspian University, Baku, Azerbaijan
[e] Department of Physics, College of Science, Princess Nourah bint Abdulrahman University, P.O. Box 84428, Riyadh, 11671, Saudi Arabia

© 2025 The Author(s). Published by the Royal Society of Chemistry

Open Access Article. Published on 28 October 2025. Downloaded on 2/12/2026 8:07:39 AM.
This article is licensed under a Creative Commons Attribution 3.0 Unported Licence.

In this study, Ca_2MgWO_6 (CMW) double perovskite tungstate phosphor was chosen as the host matrix primarily due to its distinctive crystal structures, favourable synthesis conditions, and exceptional thermal and chemical stabilities. Under ultraviolet excitation, the photoluminescence (PL) emission spectrum of the CMW exhibits broad emission bands spanning 400–700 nm. These broadband emissions originate from charge transfer transitions between the 2p orbitals of oxygen and the empty 5d orbitals of tungsten within the $[WO_6]$ octahedral groups. Such transitions are characteristics of self-activated tungstate hosts, where intrinsic luminescence arises from the functional group itself rather than from external dopants. Furthermore, charge transfer transitions in the ultraviolet (UV) region enhance the luminescence of RE centers.[28,29] Recent studies on tungstate phosphors include $NaLaMgWO_6$:Eu^{3+},[30] Lu_2WO_6:Sm^{3+},[31] Ca_3WO_6:Eu^{3+},[32] Ba_2CaWO_6:Mn^{4+},[33] Sr_2CaWO_6:Dy^{3+},[34] Ba_2MgWO_6:Ni^{2+},[35] and Ca_2MgWO_6:Tm^{3+}.[36] Among the various RE dopants, Tb^{3+} ions have been selected as activators due to their characteristic green emission in the visible region, which arises from the $^5D_4 \rightarrow {}^7F_j$ ($j = 1, 2, 3, 4, 5, 6$) electronic transitions. In addition, Tb^{3+} ions exhibit strong absorption bands resulting from spin-allowed 4f–5d transitions. By appropriately tailoring the host lattice, it is feasible to enhance the luminescent performance.[37–39] Some recently reported studies with Tb^{3+} as the optical activator include $Y_3Al_5O_{12}$:Tb^{3+},[40] BaB_2O_4:Tb^{3+},[41] $LaBO_3$:Tb^{3+},[42] $AgLa(PO_3)_4$:Tb^{3+},[43] $KCaF_3$:Tb^{3+},[44] Li_2SiO_3:Tb^{3+},[45] $Li_2NaBP_2O_8$:Tb^{3+},[46] and $Mg_3Gd_2Ge_3O_{12}$:Tb^{3+}.[47] A comprehensive survey of existing studies indicates that systematic studies on Tb^{3+}-doped Ca_2MgWO_6 phosphors are extremely limited. This gap in previous studies highlights the novelty of the present investigation and underscores the importance of exploring the luminescence mechanisms, energy transfer pathways, and concentration-dependent behaviour of this phosphor system. To bridge this research gap, a series of CMW:$x$$Tb^{3+}$ phosphors (x = 2, 4, 6, 8, and 10 mol%) were synthesized using the solid-state reaction method and systematically characterized. The study involved an in-depth analysis of their structural, thermal, and photoluminescent properties to assess their viability for use in high-temperature lighting and temperature sensing technologies.

2. Experimental method

A series of novel terbium-doped CMW:Tb^{3+} phosphor materials were synthesized *via* a solid-state reaction route. Stoichiometric proportions of calcium carbonate (99%), magnesium oxide (99%), tungsten trioxide (99%), and terbium oxide (99.9%) were used, with the addition of 3 wt% magnesium fluoride (MgF_2) as a flux to facilitate the reaction. The precursor mixture was thoroughly homogenized by grinding for 45 minutes and subsequently subjected to pre-calcination at 600 °C for 5 hours in an alumina crucible using a muffle furnace. After naturally cooling to ambient temperature, the intermediate product was reground for another 45 minutes to ensure uniformity and then subjected to calcination at 1200 °C for 5 hours. Upon cooling to room temperature, the synthesized powders were treated with concentrated nitric acid to dissolve the residual unreacted flux. The resulting suspension was filtered to isolate the purified phosphor material.[48,49]

3. Results and discussion

3.1. Optimization of Tb^{3+} concentration

The PL behaviour of the synthesized tungstate-based phosphors was examined using a JASCO FP-800 spectrofluorometer. Initially, the excitation spectrum of the CMW phosphor doped with Tb^{3+} was recorded by monitoring the emission at 546 nm, as depicted in Fig. 1(a). Typically, the excitation spectra of

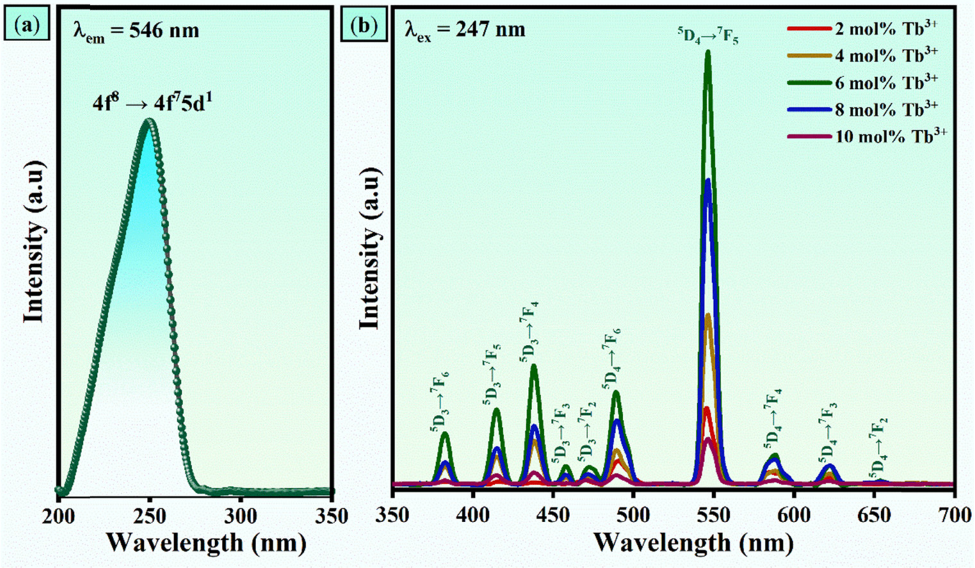

Fig. 1 (a) Excitation spectrum of the CMW phosphor doped with Tb^{3+}, monitored at 546 nm emission. (b) Emission spectra obtained under excitation at 247 nm for the prepared samples.

Open Access Article. Published on 28 October 2025. Downloaded on 2/12/2026 8:07:39 AM.
This article is licensed under a Creative Commons Attribution 3.0 Unported Licence.

Tb^{3+}-doped phosphors, when monitored within the 540–550 nm emission range, exhibit two prominent absorption regions. The first one is in a broad band between 200 and 300 nm corresponding to allowed 4f–5d transitions, and the second is between 300 and 400 nm associated with 4f–4f transitions. However, in the present case, a single dominant excitation peak was observed at 247 nm, which was attributed to a spin-allowed ($\Delta S = 0$) 4f–5d transition. Therefore, 247 nm was chosen as the optimal excitation wavelength to record the emission.[50,51]

The PL emission spectra of Ca_2MgWO_6:$x$$Tb^{3+}$ (x = 2, 4, 6, 8, and 10 mol%) phosphors, recorded under a fixed excitation wavelength of 247 nm, are illustrated in Fig. 1(b). The spectra exhibit multiple sharp and well-defined emission peaks, characteristic of f–f transitions corresponding to Tb^{3+}. Ten distinct emission bands are observed at approximately 381, 413, 436, 455, 470, 489, 546, 583, 618, and 645 nm. These emissions originate from two excited energy levels of Tb^{3+} ($^5D_3$ and $^5D_4$) and correspond to transitions $^5D_3 \rightarrow {}^7F_6$, $^5D_3 \rightarrow {}^7F_5$, $^5D_3 \rightarrow {}^7F_4$, $^5D_3 \rightarrow {}^7F_3$, $^5D_3 \rightarrow {}^7F_2$, $^5D_4 \rightarrow {}^7F_6$, $^5D_4 \rightarrow {}^7F_5$, $^5D_4 \rightarrow {}^7F_4$, $^5D_4 \rightarrow {}^7F_3$, and $^5D_4 \rightarrow {}^7F_2$ respectively.[52,53] The emissions arising from the $^5D_3$ level are typically located in the near-ultraviolet to blue region, while those from the $^5D_4$ level dominate the green-yellow-red region of the visible spectrum. A detailed summary of the excitation and emission processes between the Tb^{3+} energy levels is depicted in Fig. 2.

The systematic increase in PL intensity with increasing Tb^{3+} concentration, up to 6 mol%, can be attributed to the increased probability of radiative recombination due to the greater number of optically active Tb^{3+} centers incorporated within the host lattice. This trend reflects the enhanced energy transfer and efficient excitation of Tb^{3+} ions. However, as the concentration of Tb^{3+} ions exceeds 6 mol%, a subsequent decrease in emission intensity is observed. This reduction is ascribed to concentration quenching, which occurs due to non-radiative (NR) energy transfer mechanisms, such as cross-relaxation (CR), among closely spaced activator ions. These processes become increasingly significant at higher dopant concentrations, leading to luminescence quenching. Consequently, 6 mol% Tb^{3+} is identified as the optimum concentration that yields the maximum PL output. Beyond this optimal level, the NR losses dominate the benefits of higher activator density, thus defining the upper limit for efficient luminescent performance in the CMW:Tb^{3+} phosphor system.[54]

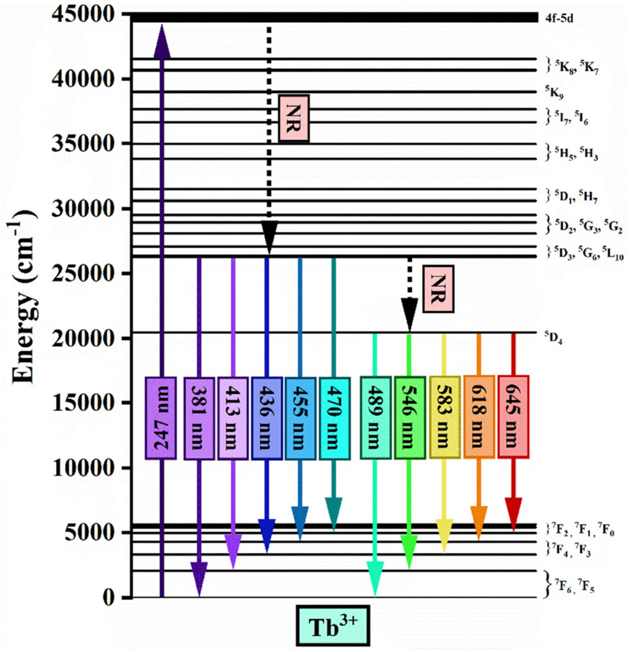

Fig. 2 Energy level of the Tb^{3+} ion in the CMW:Tb^{3+} phosphors.

For the given phosphor system, the CR process is given by[55]

$$^5D_3 + {}^7F_6 \rightarrow {}^5D_4 + {}^7F_0.$$

The proximity of the energy levels between the $^5D_3 \rightarrow {}^5D_4$ ($\sim$5900 cm^{-1}) and $^7F_6 \rightarrow {}^7F_0$ ($\sim$6000 cm^{-1}) transitions in Tb^{3+} ions facilitates a CR process between two neighbouring Tb^{3+} ions. In this mechanism, the NR relaxation of an excited electron from the $^5D_3$ to the $^5D_4$ level in one ion is coupled with the simultaneous excitation of an electron from the $^7F_6$ to the $^7F_0$ level in a neighbouring ion. The electron at the $^7F_0$ state subsequently relaxes to the ground state *via* NR pathways. As the concentration of Tb^{3+} ions increases, the probability of such CR interactions rises, resulting in an enhanced population of the $^5D_4$ state. Furthermore, energy migration among Tb^{3+} ions can occur, where excitation energy from an ion in the $^5D_4$ state is transferred to a neighbouring ion in the ground state either by exchange interaction (EI) or multipole-multipole interaction (MMI).[56]

To determine the predominant mechanism behind the energy transfer between Tb^{3+} ions, the critical distance for energy transfer (R_c) is determined. It is defined as the separation between Tb^{3+} ions at which the non-radiative and radiative energy transfers have equal probability. This parameter is crucial because it distinguishes the operative mechanism behind concentration quenching. If $R_c < 5$Å, exchange interactions typically dominate, while multipolar interactions become significant at distances greater than 5 Å.[57] R_c is calculated using the following equation:[58]

$$R_c \approx 2\left(\frac{3V}{4\pi x_c N}\right)^{\frac{1}{3}}, \tag{1}$$

where x_c = 0.06, V denotes the volume of the unit cell and N represents the total number of cation sites available within the unit cell. By substituting the values, we obtain R_c as 15.46 Å. Therefore, luminescent quenching is due to MMI.

Notably, MMI can be categorized into three distinct types of interactions: dipole–dipole (d–d), dipole–quadrupole (d–q), and quadrupole–quadrupole (q–q). To determine the dominant MMI, we use a simplified Dexter's equation:[59]

$$\mathrm{Log}_e\left(\frac{I}{x}\right) = -\frac{Q}{3}\log_e(x) + K, \tag{2}$$

where I represents the PL intensity for various concentrations of Tb^{3+} ion (x = 2, 4, 6, 8, 10 mol%) and K is a numerical constant. Q denotes a parameter that is essential to determine the nature of MMI, and it can take the values 6, 8, or 10 for d–d, d–q, and q–q interactions, respectively.[60] The determination of

© 2025 The Author(s). Published by the Royal Society of Chemistry

Open Access Article. Published on 28 October 2025. Downloaded on 2/12/2026 8:07:39 AM.
This article is licensed under a Creative Commons Attribution 3.0 Unported Licence.

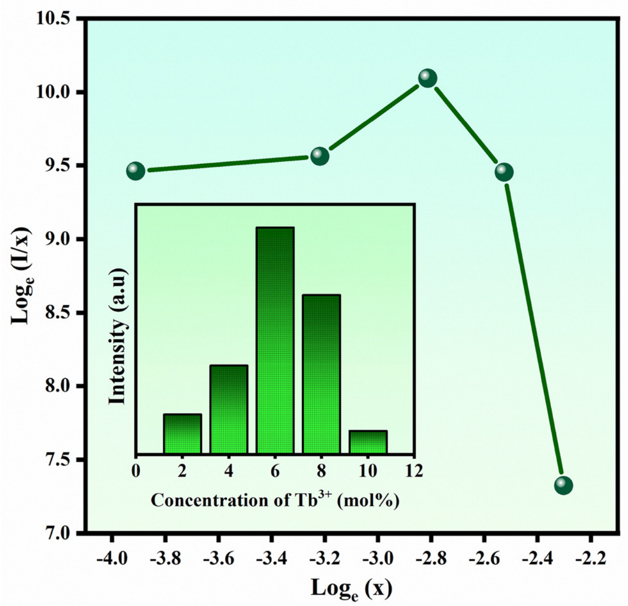

Fig. 3 Determination of the dominant multipolar interaction from the variation in PL intensity of the 546 nm peak (shown in the inset).

MMI involves plotting a graph of $\log_e\left(\frac{I}{x}\right)$ *versus* $\log_e(x)$ and performing a linear fit, as displayed in Fig. 3. It is evident from eqn (2) that the slope of the linear fit must be equal to $-\frac{Q}{3}$. As depicted in Fig. 3, we performed a linear fit for x = 6 mol% and x = 8 mol%, which yielded a slope of −2.22. Therefore, the Q value is 6.66; hence, it can be concluded that the dominant MMI for concentration quenching is the d–d interaction.

3.2. Structural and morphological properties of the optimized phosphor

Although the successful synthesis of the CMW host and its doped systems has already been established, X-ray diffraction (XRD) analysis was conducted to confirm the formation of the CMW: 6 mol% Tb^{3+} phosphor. Fig. 4(a) displays the resulting XRD patterns, which were compared with the pure CMW and standard reference patterns. The observed diffraction peaks closely match those of the reference, indicating the successful crystallization and phase purity of the synthesized phosphor system.

To evaluate the feasibility of the successful substitution of host cations by the dopant ion, we calculated the acceptable percentage difference in ionic radii (R_a) between the dopant and the target host ions.[61] If R_{Tb} denotes the ionic radius of Tb^{3+}, R_h represents the ionic radii of the host cations (Ca^{2+} and Mg^{2+}) for a given coordination number (CN). Then, the acceptable percentage difference in ionic radii is given by[62]

$$R_a = \frac{|R_h - R_{Tb}|}{R_h} \times 100\%. \tag{3}$$

According to established criteria, effective substitution occurs when $R_a < 30\%$.[63] Using Shannon's ionic radii data, we calculated the R_a values. The results are summarized in Fig. 4(b).

As illustrated in Fig. 4(b), the calculated R_a values between Ca^{2+} and Tb^{3+} range from 4% to 7.7%, while the corresponding range for Mg^{2+} and Tb^{3+} pair is 28.19–44.4%, respectively. Based on the substitution criterion of $R_a < 30\%$, we can conclude that Tb^{3+} is more likely to substitute effectively at the Ca^{2+} site than at the Mg^{2+} site. Furthermore, the ionic radius of Tb^{3+} is comparable to that of Ca^{2+}, and we did not observe any shift in the XRD patterns.[64]

Next, Rietveld refinement was performed on pure CMW phosphor and CMW doped with 6 mol% Tb^{3+} using FullProf software. Fig. 5(a) and (c) show the results of the successful refinement, while Fig. 5(b) and (d) illustrate the unit cell constructed using the refined crystallographic parameters. We provide the outcomes of Rietveld refinement in Table 1. The data in the table clearly indicate that the unit cell volume of

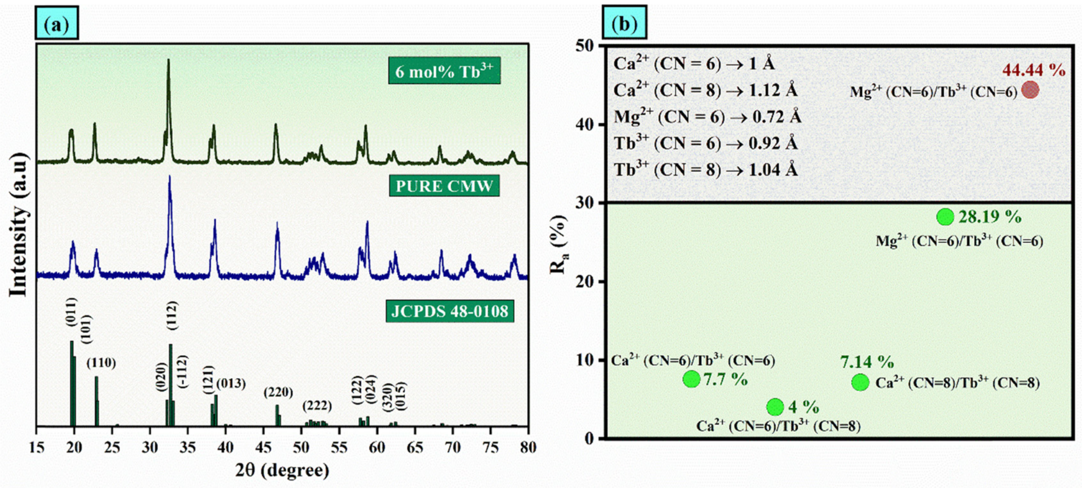

Fig. 4 (a) XRD patterns of CMW and optimized CMW: 6 mol% Tb^{3+} phosphors in comparison with JCPDS file #48-0108. (b) Acceptable percentage difference in the radius for Ca^{2+}/Tb^{3+} and Mg^{2+}/Tb^{3+} pairs.

Open Access Article. Published on 28 October 2025. Downloaded on 2/12/2026 8:07:39 AM. This article is licensed under a Creative Commons Attribution 3.0 Unported Licence.

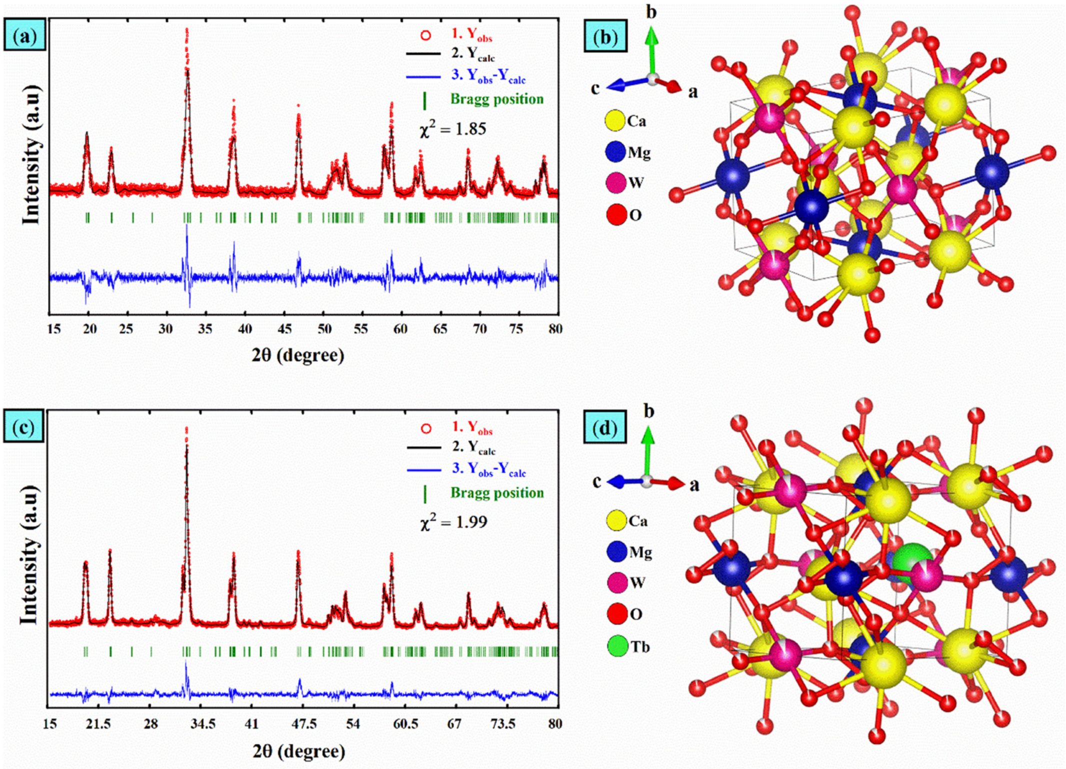

Fig. 5 (a) Results of the Rietveld refinement for CMW. (b) Unit cell of CMW drawn using the refined data. (c) Results of the Rietveld refinement for CMW:6 mol% Tb^{3+}. (d) Unit cell of CMW:6 mol% Tb^{3+} drawn using the refined data.

Table 1 Comparison of Rietveld refinement results for CMW:Tb^{3+} (6 mol%) phosphor with pure CMW

Parameter	CMW	CMW:6 mol% Tb^{3+}	CMW (data from #48-0108)
Crystal system	Monoclinic	Monoclinic	Monoclinic
Lattice parameters	α = 90°	α = 90°	α = 90°
	β = 90.070°	β = 90.073°	β = 90.092°
	γ = 90°	γ = 90°	γ = 90°
	a = 5.43243 Å	a = 5.41938 Å	a = 5.41990 Å
	b = 5.55415 Å	b = 5.54704 Å	b = 5.54790 Å
	c = 7.73257 Å	c = 7.71990 Å	c = 7.7147 Å
Volume	233.311 $Å^3$	232.0719 $Å^3$	231.9738 $Å^3$
R_p	15.6	19.5	—
R_{exp}	14.16	14.45	—
R_{wp}	19.3	20.4	—
χ^2	1.85	1.97	—

the doped CMW phosphor decreases, providing further evidence for the successful substitution of Ca^{2+} ions with Tb^{3+} ions.

Furthermore, we analyzed the morphological properties of the optimized phosphor using a scanning electron microscope (SEM). Fig. 6(a)–(c) depicts the SEM image, EDAX spectra, and the elemental mapping for the optimized phosphor, respectively. The SEM micrograph indicates that the synthesized particles possess irregular and agglomerated morphologies and lack distinct grain boundaries, a characteristic commonly observed in materials prepared *via* the solid-state reaction route.[65] To corroborate the morphological analysis, energy dispersive X-ray spectroscopy (EDS) was conducted to determine the elemental composition of the synthesized phosphor, with the corresponding EDS spectrum depicted in Fig. 6(b). The analysis confirms the host lattice elements along with the rare-earth dopant Tb^{3+}. Furthermore, elemental mapping, as shown in Fig. 6(c), was performed to evaluate the distribution of the constituent elements. The uniform distribution observed for both the host and dopant elements throughout the sample confirms the chemical homogeneity of the optimized CMW:6 mol% Tb^{3+} phosphor.[66]

3.3. Reflectance studies of the optimized phosphor

Fig. 7(a) illustrates the UV-Vis-NIR reflectance and absorbance spectra of the optimized phosphor, recorded using a PerkinElmer Lambda 900 spectrophotometer. Both spectra exhibit five distinct absorption features that are characteristic of Tb^{3+} ions. These peaks, located at approximately 487, 1732, 1801, 1979, and 2210 nm, correspond to the electronic transitions from the ground state $^7F_6$ to the excited states $^5D_4$, $^7F_0$, $^7F_1$, $^7F_2$, and $^7F_3$, respect.[67]

Using the UV-Vis-NIR spectra, we can identify the nature of the bonding between Tb^{3+} ions and the phosphor host by calculating the covalency (δ). It is calculated using the following relation:[68]

$$\delta = \frac{1-\beta_{avg}}{\beta_{avg}}, \tag{4}$$

© 2025 The Author(s). Published by the Royal Society of Chemistry

Open Access Article. Published on 28 October 2025. Downloaded on 2/12/2026 8:07:39 AM.
This article is licensed under a Creative Commons Attribution 3.0 Unported Licence.

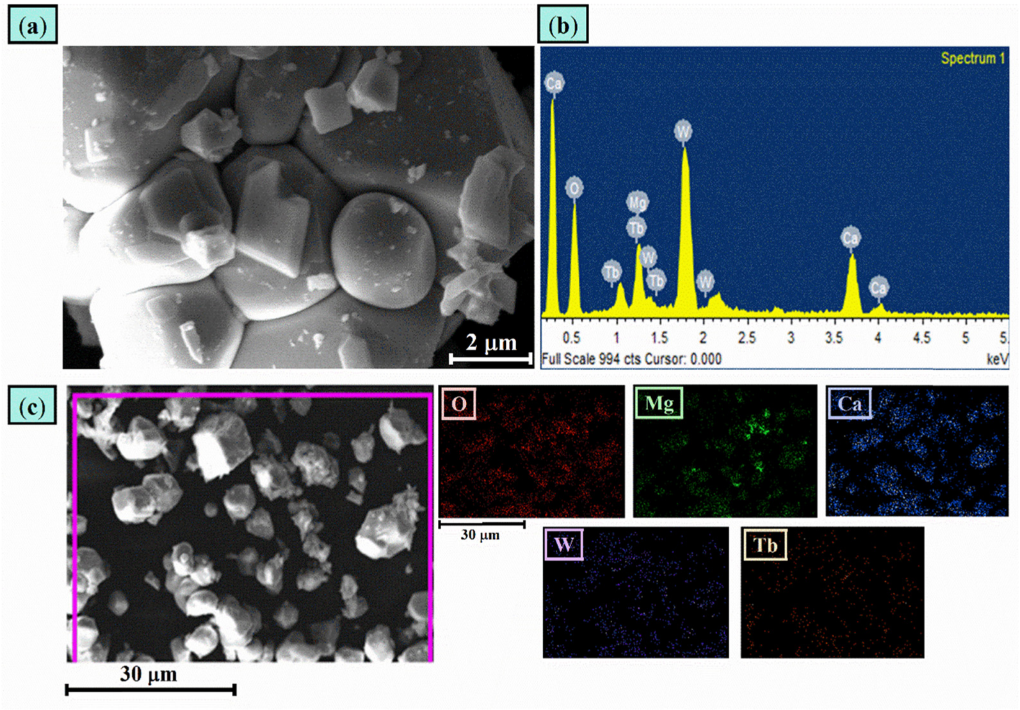

Fig. 6 (a) SEM image. (b) EDAX spectra. (c) Elemental mapping for the CMW:xTb^{3+} (x = 6 mol%) phosphor.

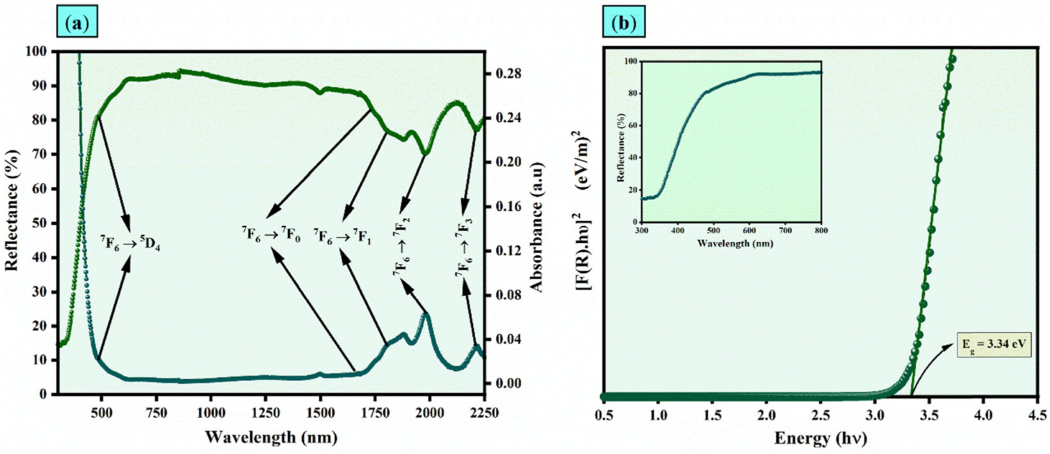

Fig. 7 (a) UV–vis-NIR spectra of the CMW:xTb^{3+} (x = 6 mol%) phosphor. (b) Optical band gap calculation for the CMW:xTb^{3+} (x = 6 mol%) phosphor using Tauc plot, with the variation in reflectance shown in the inset.

where β_{avg} is known as the average nephelauxetic ratio, and it is calculated using the following equation:[69]

$$B_{avg} = \frac{1}{N}\sum \frac{\nu_c}{\nu_a},$$

where N denotes the number of absorption bands, ν_c and ν_a denotes the energies corresponding to the transition for Tb^{3+} in the host and the aqueous environment, respectively. As depicted in Table 2, we listed ν_c and ν_a values for individual transitions and evaluated the covalency.

It is well recognized that a negative value δ indicates an ionic nature in metal–ligand bonding, whereas a positive δ suggests a covalent nature. In the present case, since δ is found to be negative, the bonding nature is inferred to be ionic. This observation aligns well with recent reports on terbium-doped systems, where similar ionic bonding characteristics have been observed.[70–72]

UV-Vis-NIR spectroscopy also serves as a valuable tool for estimating the optical band gap (E_g) of a material typically through the use of Tauc's relation. This method establishes a relationship between the photon energy (E) and E_g using the

Open Access Article. Published on 28 October 2025. Downloaded on 2/12/2026 8:07:39 AM.
This article is licensed under a Creative Commons Attribution 3.0 Unported Licence.

Table 2 Estimation of β_{avg} and δ for 6 mol% Tb^{3+} using the UV-vis-NIR data

S. no	$^7F_6 \rightarrow$	ν_c (cm^{-1})	N_a (cm^{-1})	$\frac{\nu_c}{\nu_a}$
1	$^5D_4$	20 552	20 500	1.0026
2	$^7F_0$	5779	5700	1.0138
3	$^7F_1$	5558	5440	1.0216
4	$^7F_2$	5058	5038	1.0039
5	$^7F_3$	4529	4400	1.0293

β_{avg} = 1.0142 and δ = −0.0140

Kubelka–Munk function, $F(R)$. The expression is formulated as follows:[73]

$$[F(R)\cdot E]^m = B(E - E_g) \quad (5)$$

In this expression, B is a numerical constant, and the exponent m depends on the nature of the transition: m = 2 for direct allowed transitions and m = 0.5 for indirect allowed transitions. The Kubelka–Munk function, $F(R)$, is calculated using the reflectance (R) values using the following equation:[74]

$$F(R) = \frac{(1-R)^2}{2R}$$

The optical band gap was determined by constructing a Tauc plot, in which $[F(R)\cdot E]^m$ is plotted against the photon energy (E). The band gap is extracted from the x-intercept of the linear portion of the curve, as depicted in Fig. 7(b). Here, we observed better linear fitting for m = 2, indicating that the optimized phosphor exhibits direct band gap behaviour. The corresponding optical band gap is estimated to be 3.34 eV. Next, the refractive index (n) of the phosphor can be estimated from its optical band gap energy using an empirical relation proposed by Alkathiri.[75] It is given by

$$n = 4.23 - \frac{0.98E_g - 6.37E_g^2 + 10.27E_g^3}{1 - 5.75E_g + 7.34E_g^2 + 2.73E_g^3}.$$

After substituting the value of E_g, the refractive index was found to be 2.33.

3.4. Analysis of temperature-dependent PL spectra

Temperature-dependent photoluminescence (TDPL) measurements of the optimized phosphor were carried out in the temperature range of 303–483 K under 247 nm excitation using an Agilent Cary eclipse fluorescence spectrophotometer. The corresponding variation in TDPL intensity for all emission peaks is summarized in Fig. 7(b) and 8(a), and its inset. It is evident that as the temperature increases, an enhancement in emission intensities is observed at 489, 546, 583, and 618 nm. However, intensities for the peaks at 413 and 436 nm increase up to 363 K and then progressively decrease. Among these, the prominent green emission peak at 546 nm shows a strong response, with its intensity at 483 K reaching approximately 2.42 times that recorded at room temperature.

A reduction in the TDPL intensity is observed in most of the RE-doped phosphor systems due to the increased thermally activated NR transitions. However, the unusual variation observed in our case can be attributed to the thermal trapping and de-trapping behaviour of charge carriers within localized states in the material. For the 413 and 436 nm, as the temperature increases from 303 K to 323 K, weakly localized charge carriers, while relaxing back to the ground state, can become thermally activated and subsequently trapped in deeper, strongly localized states. This trapping process leads to partial storage of the excitation energy within these defect sites, thereby reducing the available energy for radiative transitions. Beyond 323 K, increasing thermal energy allows charge carriers to reach thermal equilibrium with the host lattice and access higher-energy localized states. As the temperature further rises to 383 K, these carriers gain sufficient energy to become progressively mobile. During this process, they tend to relax to the ground state *via* radiative transitions. The resulting enhancement in emission intensity observed in the 323–383 K range is attributed to both direct band-to-band transitions from the excited state to the ground state and the radiative recombination of thermally activated charge carriers.[76] This thermal quenching phenomenon can be comprehensively described using the

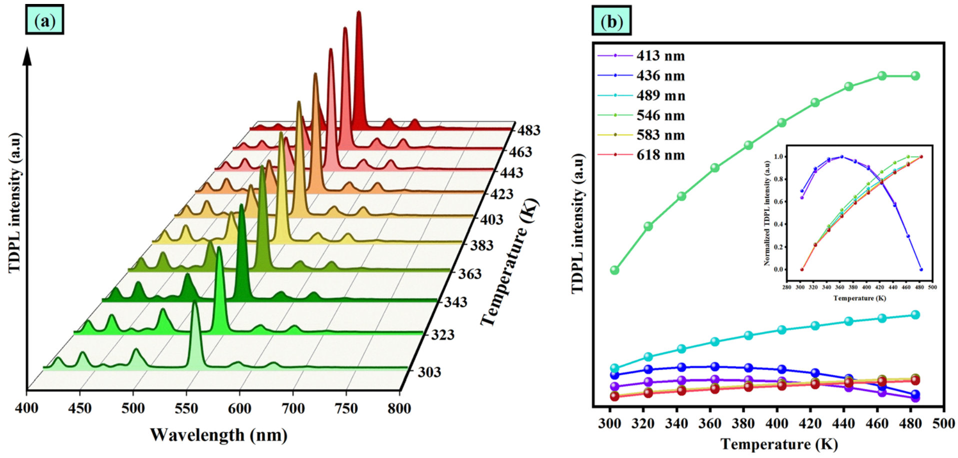

Fig. 8 (a) TDPL spectra for the CMW:xTb^{3+} (x = 6 mol%) phosphors for λ_{ex} = 247 nm. (b) Variation in TDPL intensity for the characteristic Tb^{3+} peaks with normalized TDPL intensity as shown in the inset.

Open Access Article. Published on 28 October 2025. Downloaded on 2/12/2026 8:07:39 AM.
This article is licensed under a Creative Commons Attribution 3.0 Unported Licence.

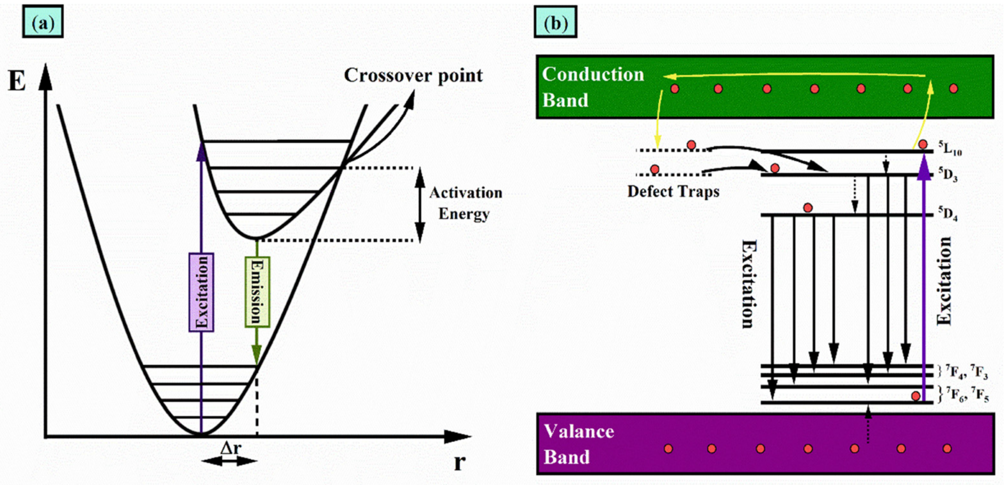

Fig. 9 (a) Configuration coordinate diagram. (b) TDPL mechanism for the optimized phosphor.

configurational coordinate model, as illustrated in Fig. 9(a). With increasing temperature, the lateral displacement (Δr) between the equilibrium positions of the ground and excited electronic states becomes larger due to increased lattice vibrations. As a result, the potential energy curves of the ground and excited states intersect at a point above the minimum of the excited state. Under these conditions, electrons occupying higher vibrational levels in the excited state can undergo non-radiative relaxation directly to the ground state through this intersection point, bypassing radiative emission. This process becomes increasingly probable at elevated temperatures, where thermal energy facilitates such transitions. Consequently, a significant portion of the excited electrons lose energy non-radiatively, leading to a marked reduction in emission intensity at high temperatures for peaks at 489, 583, and 618 nm throughout the temperature range.[77]

The continuous enhancement in TDPL intensity observed at 546 nm can be attributed to the formation of defect complexes, such as $\mathrm{Tb_{Ca}} + \mathrm{V''_{Ca}} + \mathrm{V_O}$, which act as electron-trapping centers with varying trap depths, as previously reported by Chen *et al.*[78] These defect-related traps effectively capture and store excitation energy, subsequently facilitating energy transfer to the $^5D_3$ excited states of the Tb^{3+} ions. The observed increase in TDPL emission intensity is thus ascribed to efficient thermal-assisted energy transfer from shallow traps to the $^5D_3$ energy levels. Despite the possibility of increased NR transitions at elevated temperatures, the presence of a higher density of deep trap states appears to compensate by supplying additional energy to the Tb^{3+} ions. This mechanism contributes to enhanced luminescence performance at higher temperatures. Chen *et al.* further proposed that the enhancement in PL intensity at room temperature originates from thermally assisted energy transfer from shallow defect traps to the $^5D_3$ level of Tb^{3+} ions. At higher temperatures, deeper defect levels become thermally activated, providing a continuous supply of charge carriers to the $^5D_3$ state, which compensates for NR losses and contributes to the remarkable thermal stability of the temperature-dependent luminescence. Furthermore, the carrier excitation, trapping, and release mechanisms are conceptually illustrated in the schematic diagram of the phosphor in Fig. 9(b). Upon excitation, electrons in the ground state are promoted to the $^5L_{10}$ level of Tb^{3+} ions, followed by rapid NR relaxation to the $^5D_3$ level, which subsequently undergoes radiative transitions to the ^7F_J states, resulting in characteristic emissions. In addition to this primary excitation pathway, a fraction of electrons can be thermally promoted into the conduction band, where they become trapped at defect sites of varying depths. With increasing temperature, these trapped electrons are gradually released and recombine radiatively through the $^5D_3$ level of Tb^{3+} ions, effectively compensating for the thermally induced NR losses. At lower temperatures, the release of carriers from shallow traps predominantly supports PL enhancement, while at higher temperatures, deeper traps become thermally activated, contributing to sustained luminescence stability through progressive carrier release and energy transfer processes.

Fig. 10(a)–(j) illustrates the TDPL decay profiles recorded at an emission wavelength of 546 nm under excitation wavelengths of 247 nm. We analyzed the decay behaviour using a bi-exponential fitting model, as described using the following equation:[79]

$$I = A_0 + A_1 \exp\left(-\frac{t}{\tau_1}\right) + A_2 \exp\left(-\frac{t}{\tau_2}\right),$$

where τ_1 and τ_2 represent the decay lifetimes, while A_1 and A_2 denote the coefficients obtained from the fitting process.

The average decay lifetime (τ_{avg}) corresponding to the bi-exponential decay fit was determined using the following expression:[80]

$$\tau_{\mathrm{avg}} = \frac{A_1{\tau_1}^2 + A_2{\tau_2}^2}{A_1\tau_1 + A_2\tau_2}$$

The parameters A_1, A_2, τ_1, τ_2 and τ_{avg} are presented in Table 3. Here, we observed a decrease in the decay lifetime

Open Access Article. Published on 28 October 2025. Downloaded on 2/12/2026 8:07:39 AM.
This article is licensed under a Creative Commons Attribution 3.0 Unported Licence.

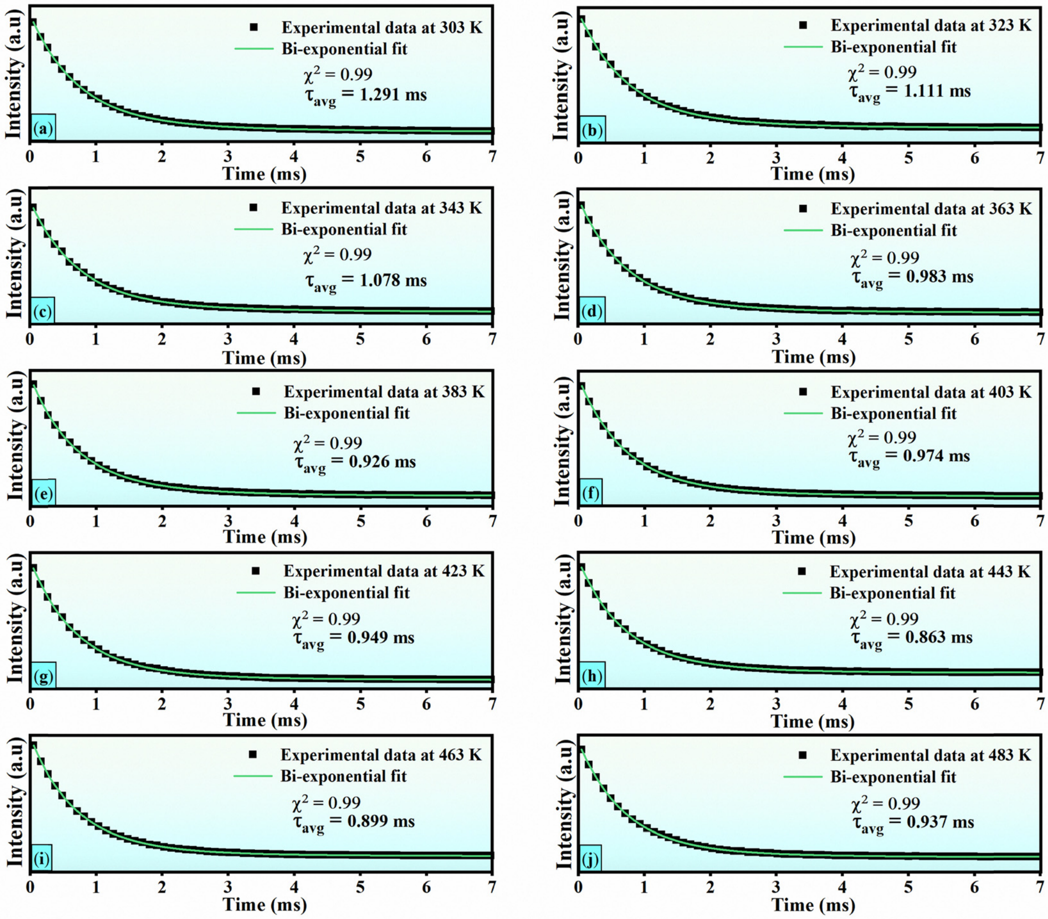

Fig. 10 (a)–(j) Decay curve for the optimized phosphor at different temperatures fitted with a bi-exponential function.

with temperature due to the presence of additional NR pathways that contribute to the overall decay process.[81]

As anticipated, the TDPL lifetime of the optimized phosphor exhibits a pronounced temperature dependence, indicating its strong potential for fluorescence thermometry applications. As shown in Table 3, τ_1 decreases gradually with increasing temperature, while τ_2 exhibits a more rapid decline. This behaviour can be attributed to the predominance of thermally assisted non-radiative processes, likely originating from self-trapped excitons transferring energy to defect states.[82]

Table 3 Parameters obtained from the bi-exponential fit

T	A_1	τ_1 (ms)	A_2	τ_2 (ms)	τ_{avg} (ms)
303	271.581	0.706	31.472	2.641	1.291
323	340.621	0.689	47.035	2.108	1.111
343	401.976	0.699	45.883	2.154	1.078
363	440.172	0.675	68.026	1.750	0.983
383	455.652	0.634	112.202	1.447	0.926
403	550.751	0.678	63.517	1.894	0.974
423	577.790	0.663	80.004	1.738	0.949
443	483.961	0.589	218.511	1.169	0.863
463	631.796	0.655	104.119	1.532	0.899
483	681.080	0.670	75.567	1.821	0.937

4. Applications of the optimized phosphor

4.1. High temperature lighting applications

First, we evaluate the local coordination environment of the Tb^{3+} ions in the host lattice by calculating the asymmetry ratio from the emission spectrum. This ratio is defined as the intensity of the electric dipole transition ($^5D_4 \rightarrow {}^7F_5$) relative to the magnetic dipole transition ($^5D_4 \rightarrow {}^7F_6$).[83] A value greater than unity indicates that the dopant ions occupy non-centrosymmetric sites within the crystal structure. The variation in the asymmetry ratio with Tb^{3+} concentration is presented in Fig. 11(a). For the prepared phosphor samples, the ratio ranges from 3.4 to 5.2, confirming a significantly distorted local environment. This asymmetry is primarily responsible for the intense and sharp green emission observed at 546 nm.[84]

As discussed in the previous section, the optimized phosphor exhibited a notable enhancement in the TDPL intensity of its dominant green emission under analysis up to 483 K. This thermally induced improvement in emission intensity suggests promising potential for high-temperature lighting applications. To further evaluate its performance, the Commission Internationale de l'Eclairage (CIE) chromaticity coordinates of the prepared phosphors (x_p, y_p) were calculated at room temperature.

© 2025 The Author(s). Published by the Royal Society of Chemistry

Open Access Article. Published on 28 October 2025. Downloaded on 2/12/2026 8:07:39 AM.
This article is licensed under a Creative Commons Attribution 3.0 Unported Licence.

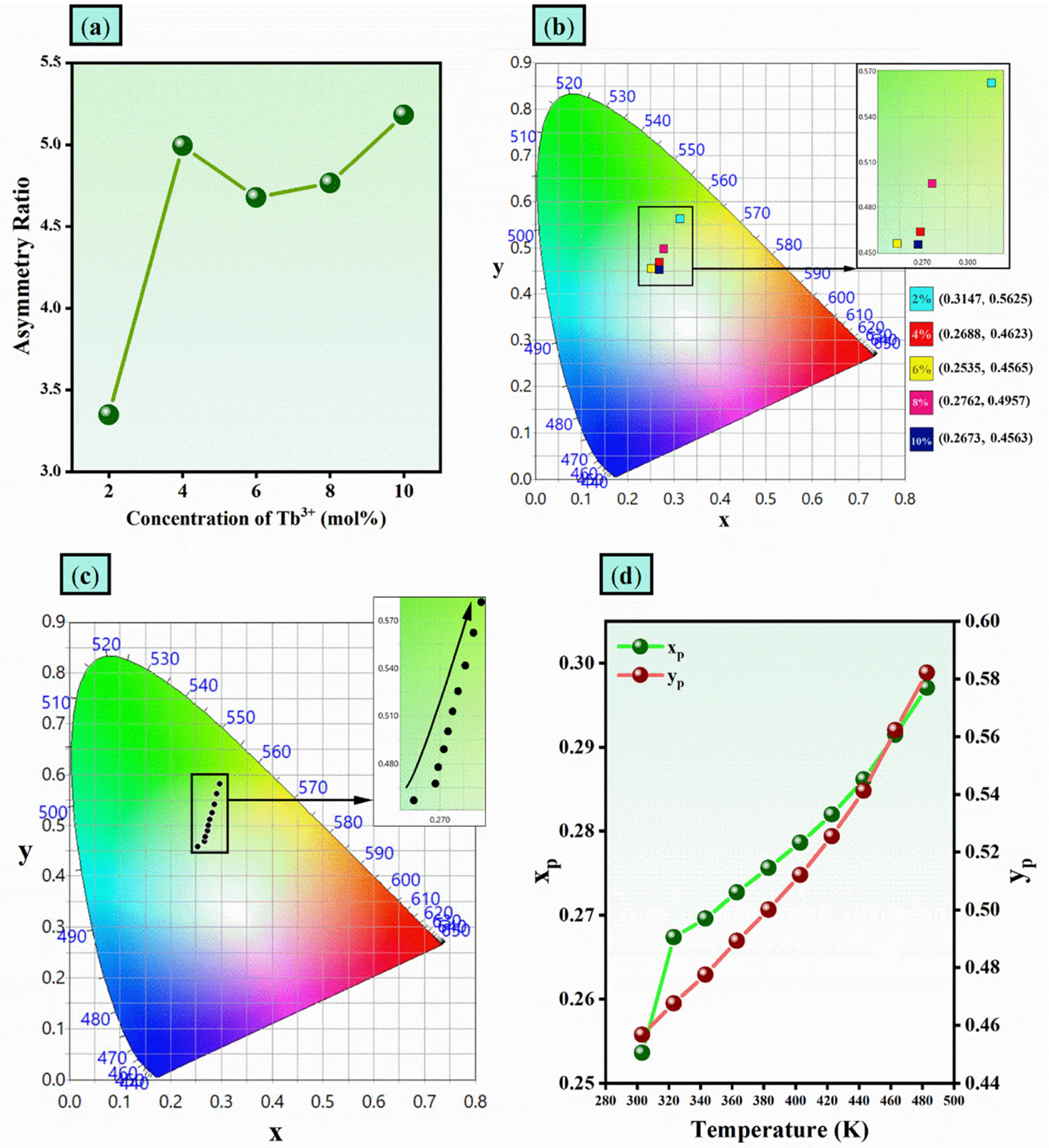

Fig. 11 (a) Variation in asymmetric ratio with Tb^{3+} concentration. (b) CIE-1931 chromaticity diagram for the synthesized phosphor samples. (c) and (d) Temperature-dependent CIE coordinates of the optimized phosphor and its variation with the temperature.

These coordinates were then mapped onto the 1931 CIE chromaticity diagram, as illustrated in Fig. 11(b). Next, we also studied the variation of the chromaticity coordinates with temperature. We plotted the coordinates in Fig. 11(c). The overall variation is shown in Fig. 11(d).

It is clear from the figures that as the temperature increases, the chromaticity coordinates shift towards the green region. To evaluate the optical stability of the phosphor, variations in the chromaticity coordinates (x_{var}, y_{var}) and the corresponding chromatic shift (ΔE) were calculated. The degree of variation in the colour coordinates was determined using the following equations:

$$x_{\mathrm{var}} = \frac{1}{n}\sum_{i=1}^{n}(x_i - \bar{x})^2,$$

$$y_{\mathrm{var}} = \frac{1}{n}\sum_{i=1}^{n}(y_i - \bar{y})^2,$$

where (x_i, y_i) represents the CIE chromaticity coordinates measured at temperature T above room temperature, while ($\bar{x}$, $\bar{y}$) represents the average values of the chromaticity coordinates over the examined temperature range. Based on the calculated data, the variance in the colour coordinates was determined to be $x_{\mathrm{var}} = 1.05 \times 10^{-4}$ and $y_{\mathrm{var}} = 15.6 \times 10^{-4}$, indicating excellent colour stability of the phosphor under thermal excitation.

Additionally, the chromaticity shift (ΔE) was determined using the following mathematical relation, which quantifies the overall displacement in colour coordinates as a function of

Open Access Article. Published on 28 October 2025. Downloaded on 2/12/2026 8:07:39 AM.
This article is licensed under a Creative Commons Attribution 3.0 Unported Licence.

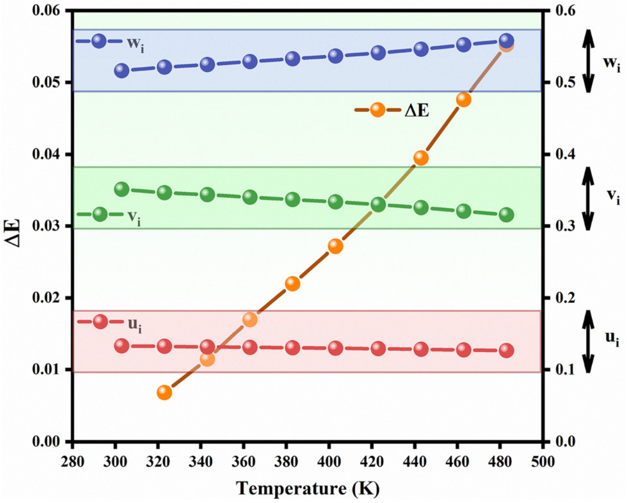

Fig. 12 Variations in u_i, v_i, w_i, and ΔE with temperature.

temperature:[85]

$$\Delta E = \sqrt{(u_i - u_o)^2 + (v_i - v_o)^2 + (w_i - w_o)^2},$$

where $u_i = \dfrac{4x_i}{3 - 2x_i + 12y_I}$, $v_i = \dfrac{9y_i}{3 - 2x_i + 12y_I}$, $w_i = 1 - u_i - v_i$ and (u_o, v_o, w_o) represents the values corresponding to room temperature. The computed value of ΔE was nearly equal to 5.5×10^{-2} at 483 K. Additionally, we showed variations in u_i, v_i, w_i, and ΔE (Fig. 12). Due to efficient green emission with incredible thermal enhancement, the optimized phosphor can be used for green light generation and the green component in high temperature white LED applications.

4.2. Temperature sensing applications

Temperature is a fundamental thermodynamic parameter that plays a pivotal role across various critical industries, including aerospace, biomedical, and food storage sectors. Conventional contact-based temperature sensors, which necessitate direct physical contact with the target object, are often susceptible to environmental disturbances during measurements. In contrast, non-contact optical temperature sensors have garnered significant attention due to their rapid response time, high sensitivity, excellent stability, strong resistance to external interference, and capability to accurately measure temperatures in micro-environments.[86,87] In this section, we studied the non-contact temperature sensing properties of optimized CMW:xTb^{3+} (x = 6 mol%) phosphor.

In order to understand the temperature sensing behaviour, we use the FIR technique, which is based on the thermally coupled energy levels at 489 and 546 nm. If I_{489} and I_{546} represent the intensity of peaks at 489 and 546 nm at temperature T, respectively, then the FIR is defined as follows:[88]

$$\text{FIR} = \frac{I_{489}}{I_{546}}$$

We computed the ratio for different temperatures, and it is plotted in Fig. 13(a). Next, we fitted FIR with the exponential, second, and third order polynomial functions, and they are given below:[89,90]

$$\text{FIR} = A_0 \exp(-A_1/T) \tag{6}$$

$$\text{FIR} = B_0 + B_1T^1 + B_2T^2 \tag{7}$$

$$\text{FIR} = C_0 + C_1T^1 + C_2T^2 + C_3T^3, \tag{8}$$

We carried out the fitting in the temperature range 303–463 K, and the results are shown in Fig. 13(b)–(d).

A better fit was observed for the polynomial fit compared to the exponential fit. Hence, the polynomial fit can be a suitable choice for temperature sensing applications of the optimized phosphors.

To validate the thermal sensing capability of the material and assess its performance, both absolute sensitivity (S_a) and relative sensitivity (S_r) were calculated. Here, S_r provides insight into the sensor's effectiveness over the investigated temperature range, while the S_a serves as an indicator of the probe's precision in detecting temperature variations. These parameters are defined as follows:[91]

$$S_a = \left|\frac{\delta}{\delta T}(\text{FIR})\right|, \tag{9}$$

$$S_r = \left|\frac{S_a}{\text{FIR}}\right| \times 100\%. \tag{10}$$

On substituting for FIR in eqn (6)–(8) in the above equations, we can obtain the equation for the sensitivities, and these equations are provided below.

For the exponential function,

$$S_a = \left|\frac{d}{dT}(\text{FIR})\right| = \text{FIR} \cdot \frac{A_1}{T^2},$$

$$S_r = \left|\frac{1}{\text{FIR}}\frac{d}{dT}(\text{FIR})\right| = \frac{A_1}{T^2}.$$

For the 2nd order polynomial function,

$$S_a = \left|\frac{d}{dT}(\text{FIR})\right| = B_1 + 2B_2T^1,$$

$$S_r = \left|\frac{1}{\text{FIR}}\frac{d}{dT}(\text{FIR})\right| = \frac{B_1 + 2B_2T^1}{B_0 + B_1T^1 + B_2T^2}$$

Finally, for the 3rd order fit,

$$S_a = \left|\frac{d}{dT}(\text{FIR})\right| = C_1 + 2C_2T^1 + 3C_3T^2,$$

$$S_r = \left|\frac{1}{\text{FIR}}\frac{d}{dT}(\text{FIR})\right| = \frac{C_1 + 2C_2T^1 + 3C_3T^2}{C_0 + C_1T^1 + C_2T^2 + C_3T^3}.$$

© 2025 The Author(s). Published by the Royal Society of Chemistry

Open Access Article. Published on 28 October 2025. Downloaded on 2/12/2026 8:07:39 AM.
This article is licensed under a Creative Commons Attribution 3.0 Unported Licence.

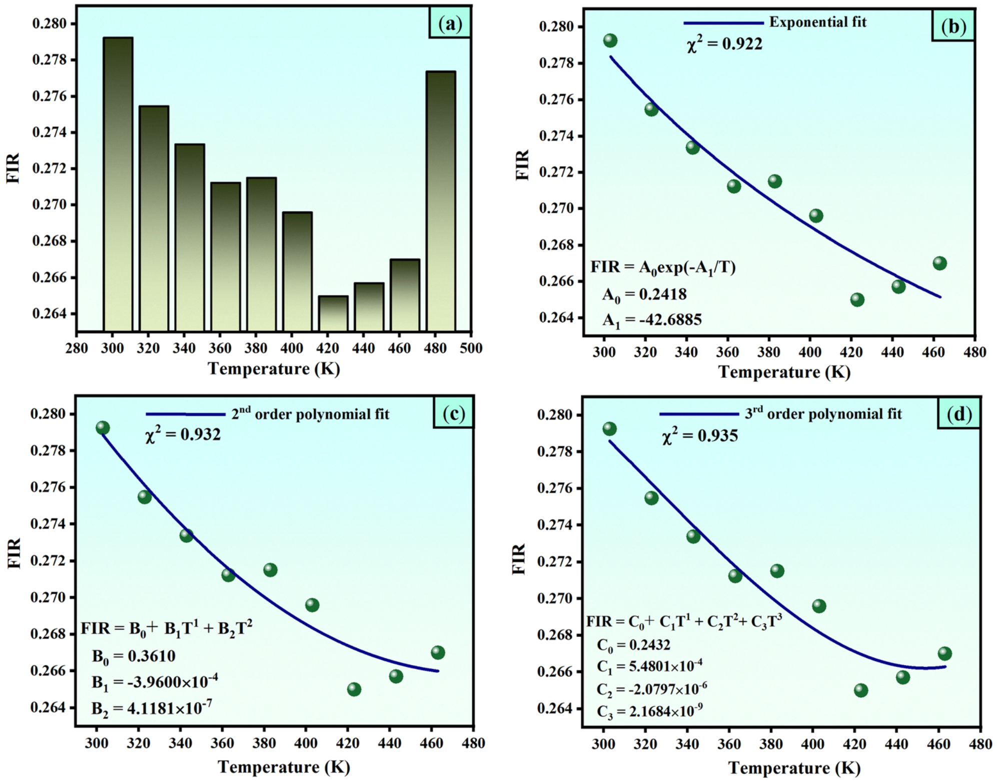

Fig. 13 (a) Variation in FIR with temperature. (b)–(d) FIR fitted with the exponential, 2nd, and 3rd order polynomial functions.

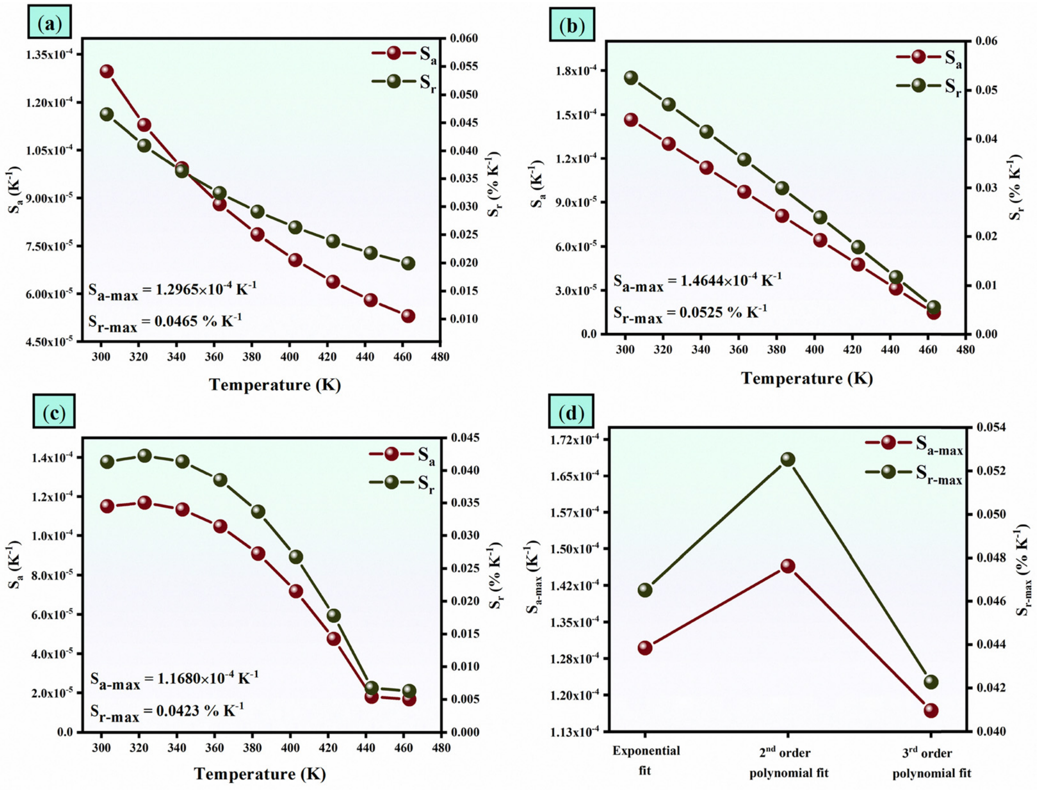

Fig. 14 (a)–(c) Variation in plot sensitivity values for exponential, 2nd, and 3rd order polynomial fit. (d) Comparison of maximum sensitivity values with respect to the fitting functions.

Open Access Article. Published on 28 October 2025. Downloaded on 2/12/2026 8:07:39 AM.
This article is licensed under a Creative Commons Attribution 3.0 Unported Licence.

Table 4 Comparison of temperature sensing performance with reported phosphors

Phosphor	Temperature (K)	$S_{\text{a-max}}$ (K^{-1})	$S_{\text{r-max}}$ (% K^{-1})	Ref.
$YbTaO_4$:Er^{3+}	300–570	0.0038	1.02	92
Y_4GeO_8:Er^{3+}, Yb^{3+}	303–573	0.0045	1.15	93
$Ba_5Y_8Zn_4O_{21}$:Yb^{3+}, Er^{3+}	293–563	0.0039	1.36	94
$Na_2GdMg_2V_3O_{12}$:Sm^{3+}	303–513	0.6650	2.12	95
$NaYF_4$:Yb^{3+}, Ho^{3+}, Tm^{3+}	295–495	0.0126	1.80	96
$NaYTiO_4$:Yb^{3+}, Tm^{3+}	303–823	0.0009	0.60	97
$Ba_{3-x}Sr_xLu_4O_9$:Tm^{3+}, Yb^{3+}	303–573	0.0015	0.88	98
$CaLaMgTaO_6$:Bi^{3+}, Er^{3+}	303–483	0.0028	1.45	99
$SrGa_2B_2O_7$:Bi^{3+}, Eu^{3+}	293–573	0.1810	1.55	100
$NaY_9Si_6O_{26}$:Ce^{3+}, Eu^{3+}	293–523	0.0328	0.95	101
$NaLaCaWO_6$:Eu^{3+}	293–448	0.0042	2.23	102
La_2LiNbO_6:Mn^{4+}, Eu^{3+}	293–498	1.0400	1.28	103
Lu_2MoO_6:Er^{3+}, Yb^{3+}, Li^+	253–423	0.0150	0.02	104
Ca_2MgWO_6:Tb^{3+}	303–463	1.4644×10^{-4}	0.05	This work

Using the above equations, S_a and S_r values are calculated, and they are plotted in Fig. 14(a)–(c). For both exponential and 2nd order polynomial fit, the maximum values of S_a and S_r were observed at 303 K. Thereafter, both S_a and S_r decrease monotonically with the increase in temperature. However, for the 3rd order fit, S_a and S_r increase with the increase in temperature to 323 K, and thereafter they decrease to 463 K.

An overall summary of the variation of the maximum absolute and relative sensitivities ($S_{\text{a-max}}$ and $S_{\text{r-max}}$) is provided in Fig. 14(d). It is important to note that, even though better fitting is observed for the 3rd order polynomial fit, the highest absolute and relative sensitivity (1.4644×10^{-4} K^{-1} and 0.05% K^{-1}) is observed in the case of the 2nd order polynomial fit. Table 4 presents a comparative analysis of the temperature sensing performance of the synthesized phosphors with those of previously reported phosphor materials. The results demonstrate that the developed phosphors possess competitive or superior thermal sensitivity, highlighting their potential as reliable candidates for optical temperature sensing applications.

5. Conclusions

In this study, Ca_2MgWO_6 phosphors doped with varying concentrations of Tb^{3+} ions were successfully synthesized *via* a high-temperature solid-state reaction route and systematically characterized. Photoluminescence studies revealed that the green emission corresponding to the $^5D_4 \rightarrow {}^7F_5$ transition intensified with increasing Tb^{3+} content, reaching a maximum at 6 mol%. X-ray diffraction confirmed the phase purity of the optimized composition, while SEM-EDAX analysis demonstrated an agglomerated microstructure with a uniform elemental distribution. TDPL measurements showed a remarkable enhancement of emission intensity of 546 nm up to 242% as the temperature increased to 483 K, indicating a negative thermal quenching behaviour. Additionally, the Ca_2MgWO_6: 6 mol% Tb^{3+} phosphor exhibited excellent optical temperature sensing performance, with maximum absolute and relative sensitivities of 1.4644×10^{-4} K^{-1} and 0.05% K^{-1}, respectively, at 303 K. The material demonstrated a wide sensing range from 303 K to 483 K, placing it among the best-performing Tb^{3+}-doped systems. These results affirm phosphor's strong potential for high-temperature solid-state lighting and non-contact optical thermometry applications.

Conflicts of interest

There are no conflicts to declare.

Data availability

Data will be made available on request.

Acknowledgements

The authors also acknowledge the financial support from the Manipal Academy of Higher Education, Manipal, India.

References

1 Y. Zhou, T. Seto and Y. Wang, *Laser Photonics Rev.*, 2023, **17**, 2200462.
2 J. Qiao, J. Zhao, Q. Liu and Z. Xia, *J. Rare Earths*, 2019, **37**, 565–572.
3 R. S. Yadav, Monika, S. B. Rai and S. J. Dhoble, *Prog. Solid State Chem.*, 2020, **57**, 100267.
4 I. G. N. Silva, A. F. Morais, L. F. M. Zambon, H. F. Brito and D. Mustafa, *Opt. Mater. (Amsterdam, Neth.)*, 2018, **76**, 48–55.
5 M. Sato, S. W. Kim, Y. Shimomura, T. Hasegawa, K. Toda and G. Adachi, *Handbook on the Physics and Chemistry of Rare Earths*, Elsevier, 2016, vol. 49, pp. 1–128.
6 J. Ballato, J. S. Lewis and P. Holloway, *MRS Bull.*, 1999, **24**, 51–56.
7 R.-J. Xie, N. Hirosaki, Y. Li and T. Takeda, *Materials*, 2010, **3**, 3777–3793.
8 P. C. Ricci, *Crystals*, 2020, **10**, 559.
9 S. E. Crawford, P. R. Ohodnicki and J. P. Baltrus, *J. Mater. Chem. C*, 2020, **8**, 7975–8006.
10 M. K. Hossain, M. H. Ahmed, M. I. Khan, M. S. Miah and S. Hossain, *ACS Appl. Electron. Mater.*, 2021, **3**, 4255–4283.
11 I. N. Bazhukova, V. A. Pustovarov, A. V. Myshkina and M. V. Ulitko, *Opt. Spectrosc.*, 2020, **128**, 2050–2068.
12 M. Gu, W. Li, L. Jiang and X. Li, *Acta Biomater.*, 2022, **148**, 22–43.
13 S. Sood, P. Kumar, I. Raina, M. Misra, S. Kaushal, J. Gaur, S. Kumar and G. Singh, *Photonics*, 2025, **12**, 454.
14 X. Wang, J. Xu, J. Yu, Y. Bu, J. Marques-Hueso and X. Yan, *Phys. Chem. Chem. Phys.*, 2020, **22**, 15120–15162.
15 R. Song, R. Wang, X. Yang, X. Bian and H. Fu, *Appl. Mater. Today*, 2024, **38**, 102246.

© 2025 The Author(s). Published by the Royal Society of Chemistry

Open Access Article. Published on 28 October 2025. Downloaded on 2/12/2026 8:07:39 AM.
This article is licensed under a Creative Commons Attribution 3.0 Unported Licence.

16 J. Chen, J. Chen, W. Zhang, S. Xu, L. Chen and H. Guo, *Ceram. Int.*, 2023, **49**, 16252–16259.

17 K. Qiang, Y. Ye, Q. Mao, F. Chen, L. Chu, M. Liu and J. Zhong, *Mater. Des.*, 2024, **241**, 112906.

18 X. Tian, X. Yin, F. Wu, C. Ji, Z. Huang, L. Zhu, F. Luo, X. Liu, J. Li, H. Peng, X. Wu, G. Li, J. Wen and H.-T. Lin, *Ceram. Int.*, 2025, **51**, 4828–4837.

19 X. Peng, J. Chen, Y. Chen, Y. Jiang, R. Wei, W. Zhou, H. Li and H. Guo, *J. Alloys Compd.*, 2021, **885**, 161010.

20 Anu and A. S. Rao, *Opt. Mater. (Amsterdam, Neth.)*, 2023, **145**, 114476.

21 M. Erdem, S. B. Cantürk and G. Eryürek, *Spectrochim. Acta, Part A*, 2022, **270**, 120854.

22 S. Lig, H. Muji, Y. Zhang, X. Zhou, K. Wang, Z. Wang, Q. Tian and K. Chao, *Ceram. Int.*, 2024, **50**, 53264–53271.

23 W. Wang, Q. Li, L. Chen, Y. Wang, R. Zhong, H. Dong, Y. Qiu, Y. Hu and X. Zhang, *J. Lumin.*, 2023, **257**, 119683.

24 Anu and A. S. Rao, *Sens. Actuators, A*, 2024, **372**, 115336.

25 L. Ma, F. Lu, Q. Yu, P. Dai, F. Hu, H. Guo and R. Wei, *Ceram. Int.*, 2023, **49**, 16681–16689.

26 W. Wang, J. Xie, Y. Zhong, T. Su, X. Li, Y. Pan, X. Wei and Y. Li, *J. Photochem. Photobiol., A*, 2025, **462**, 116223.

27 N. Rakov, F. Matias and G. S. Maciel, *Phys. B (Amsterdam, Neth.)*, 2023, **652**, 414625.

28 R. Yu, J. Wang, Z. Zhao, M. Li, S. Huo, J. Li and J. Wang, *Mater. Lett.*, 2015, **160**, 294–297.

29 J. Zhang, Z. Song, P. Cai and X. Wang, *Phys. Chem. Chem. Phys.*, 2023, **25**, 1565–1587.

30 Q. Liu, X. Li, B. Zhang, L. Wang, Q. Zhang and L. Zhang, *Ceram. Int.*, 2016, **42**, 15294–15300.

31 Y. Zhang, B. Ding, L. Yin, J. Xin, R. Zhao, S. Zheng and X. Yan, *Inorg. Chem.*, 2018, **57**, 507–518.

32 S. Zhang, Y. Hu, L. Chen, X. Wang, G. Ju and Y. Fan, *J. Lumin.*, 2013, **142**, 116–121.

33 Q. Mao, G. Li, X. Shen, J. Xi, L. Pei, X. Li and J. Zhong, *Ceram. Int.*, 2024, **50**, 6453–6460.

34 Y. Dai, S. Yang, Y. Shan, C.-G. Duan, H. Peng, F. Yang and Q. Zhao, *Materials*, 2019, **12**, 431.

35 X. Lu, Y. Gao, J. Chen, M. Tan and J. Qiu, *ACS Appl. Mater. Interfaces*, 2023, **15**, 39472–39479.

36 Y. Guo, H. Li, R. Pang, D. Li, L. Jiang and S. Zhang, *Ceram. Int.*, 2025, **51**, 22050–22058.

37 S. Srivastava, S. K. Behera and B. B. Nayak, *Optik*, 2021, **231**, 166411.

38 B. Ramesh, G. R. Dillip, B. Rambabu, S. W. Joo and B. D. P. Raju, *J. Mol. Struct.*, 2018, **1155**, 568–572.

39 P. C. Ricci, C. M. Carbonaro, R. Corpino, C. Cannas and M. Salis, *J. Phys. Chem. C*, 2011, **115**, 16630–16636.

40 S. Singh and D. Singh, *J. Mater. Sci.: Mater. Electron.*, 2021, **32**, 17674–17685.

41 S. Jakathamani, O. Annalakshmi, M. T. Jose and B. Venkatraman, *Radiat. Phys. Chem.*, 2021, **187**, 109544.

42 Z. Wan, D. Xu, W. She, F. Xie, Y. Feng, J. Yang, G. Liu and X. Tong, *Ceram. Int.*, 2024, **50**, 9499–9509.

43 L. Ajili, A. Selmi, A. Bourezgui, A. Elboughdiri, H. Rahmouni, N. Sdiri, R. Mnaseri, M. Férid and K. Horchani–Naifer, *Emergent Mater.*, 2023, **6**, 1059–1069.

44 R. Kameshwaran, O. Annalakshmi and P. B. Bhargav, *Ceram. Int.*, 2023, **49**, 8005–8014.

45 P. Barik, A. K. Verma, R. Kumar, V. Kumar, P. Dewangan, M. Sahu and I. P. Sahu, *Appl. Phys. A: Mater. Sci. Process.*, 2024, **130**, 391.

46 J. Zhu, J. Xiang and Y. Mao, *Optik*, 2021, **240**, 166920.

47 J. Bai, J. Zhang, C. Kong, B. Zhang, Y. Cao, Y. Wang, X. Zhang, B. Chen and K. Li, *Ceram. Int.*, 2025, **51**, 21913–21921.

48 L. Li, J. Chen, Y. Jiang, S. Xu and H. Guo, *J. Lumin.*, 2023, **258**, 119782.

49 R. Kiran, N. S. Prabhu, V. Mishra, M. I. Sayyed and S. D. Kamath, *Indian J. Phys.*, 2025, **99**, 2023–2032.

50 N. Degda, N. Patel, V. Verma, K. V. R. Murthy and M. Srinivas, *Luminescence*, 2024, **39**, e4622.

51 R. Kamal and M. Saif, *Spectrochim. Acta, Part A*, 2020, **229**, 117928.

52 J. Zhan, S. Peng, Y. Zhu, Z. Zhu, J. Liu, H. Peng, X. Meng and L. Yang, *Ceram. Int.*, 2024, **50**, 4896–4906.

53 R. Paikaray, T. Badapanda, S. Sahoo and H. Mohapatra, *Eur. Phys. J. B*, 2024, **97**, 79.

54 E. Umur, E. Bayrak, F. Arslan, S. B. Bulut, E. Baysoy, G. Kaleli-Can and B. Ayan, *Appl. Sci.*, 2023, **13**, 10269.

55 X. Zhou, S. Jiang, G. Xiang, X. Tang, X. Luo, L. Li and X. Zhou, *J. Am. Ceram. Soc.*, 2018, **101**, 3076–3085.

56 G. Blasse and A. Bril, *J. Electrochem. Soc.*, 1968, **115**, 1067.

57 D. L. Dexter, *J. Chem. Phys.*, 1953, **21**, 836–850.

58 C. M. Nandanwar, N. S. Kokode, R. M. Yerojwar and A. N. Yerpude, *Nano-Struct. Nano-Objects*, 2023, **36**, 101068.

59 V. Singh, M. Seshadri, M. Radha, C. M. Mehare, S. J. Dhoble and J. B. Joo, *J. Electron. Mater.*, 2024, **53**, 2340–2350.

60 K. Xu, L. Zhao, Y. Guo and Y. Fu, *New J. Chem.*, 2024, **48**, 11874–11885.

61 L. A. Xue, Y. Chen and R. J. Brook, *Mater. Sci. Eng., B*, 1988, **1**, 193–201.

62 N. Hussain, S. Rubab and V. Kumar, *Ceram. Int.*, 2023, **49**, 15341–15348.

63 C. Kumari, A. Kumar, S. K. Sharma and J. Manam, *Vacuum*, 2023, **207**, 111599.

64 M. Misevicius, E. Griniuk and R. Ramanauskas, *Mater. Chem. Phys.*, 2023, **306**, 128082.

65 Y. Jiang, Y. Tong, S. Chen, W. Zhang, F. Hu, R. Wei and H. Guo, *Chem. Eng. J. (Amsterdam, Neth.)*, 2021, **413**, 127470.

66 N. Miniajluk, B. Bondzior, D. Stefańska and P. J. Dereń, *J. Alloys Compd.*, 2019, **802**, 190–195.

67 M. Runowski, N. Stopikowska and S. Lis, *Dalton Trans.*, 2020, **49**, 2129–2137.

68 K. J. Albert, E. A. Rathnakumari and S. M. M. Kennedy, *J. Alloys Compd.*, 2023, **934**, 168047.

69 K. Mondal, D. K. Singh and J. Manam, *J. Alloys Compd.*, 2018, **761**, 41–51.

70 A. Jose, S. T. Sunny, T. Krishnapriya, A. R. Varghese, S. A. Oommen, A. George, S. K. Jose and P. R. Biju, *J. Mater. Sci.: Mater. Electron.*, 2024, **35**, 2246.

Open Access Article. Published on 28 October 2025. Downloaded on 2/12/2026 8:07:39 AM.
This article is licensed under a Creative Commons Attribution 3.0 Unported Licence.

71 N. Ma, Z. Luo, H. Liang, L. He, A. Lu and T. Liu, *J. Alloys Compd.*, 2024, **1003**, 175596.

72 A. Ratep and I. Kashif, *Opt. Quantum Electron.*, 2023, **55**, 559.

73 J. Klein, L. Kampermann, B. Mockenhaupt, M. Behrens, J. Strunk and G. Bacher, *Adv. Funct. Mater.*, 2023, **33**, 2304523.

74 P. Makuła, M. Pacia and W. Macyk, *J. Phys. Chem. Lett.*, 2018, **9**, 6814–6817.

75 A. A. Alkathiri, *J. Radiat. Res. Appl. Sci.*, 2024, **17**, 100783.

76 R. Gopal, A. Kumar and J. Manam, *Mater. Chem. Phys.*, 2021, **272**, 124960.

77 A. Kumar and J. Manam, *Opt. Mater. (Amsterdam, Neth.)*, 2019, **96**, 109373.

78 Y. Chen, B. Yu, J. Gou and S. F. Liu, *J. Mater. Chem. C*, 2018, **6**, 10687–10692.

79 N. Degda, N. Patel, V. Verma, M. Srinivas, K. V. R. Murthy and D. Haranath, *Luminescence*, 2023, **38**, 176–187.

80 A. Krishnan, K. Sathishkumar, O. R. Devi, S. Agrawal, A. Debnath, M. V. Arasu, T. Sundaram, K. Subramanian and R. Karunakaran, *Nanotechnol. Rev.*, 2024, **13**, 20240106.

81 L. Wu, H. Zhang, W. Zheng, X. Zhang and H. J. Seo, *Mater. Res. Bull.*, 2017, **93**, 245–250.

82 G. Li, X. Chen, M. Wang, S. Cheng, D. Yang, D. Wu, Y. Han, M. Jia, X. Li, Y. Zhang, C. Shan and Z. Shi, *Adv. Mater. (Weinheim, Ger.)*, 2023, **35**, 2305495.

83 Y. Wang, P. Darapaneni, O. Kizilkaya and J. A. Dorman, *Inorg. Chem.*, 2020, **59**, 2358–2366.

84 S. Thomas, B. Baby, J. Jose, A. V. Lizbathu, P. R. Biju and C. Joseph, *J. Lumin.*, 2023, **264**, 120188.

85 S. Xu, J. Fu, X. Liu, M. Yuan, C. Zhang, H. Wang, G. Liu and S. Cui, *Ceram. Int.*, 2023, **49**, 5228–5238.

86 C. D. S. Brites, R. Marin, M. Suta, A. N. Carneiro Neto, E. Ximendes, D. Jaque and L. D. Carlos, *Adv. Mater. (Weinheim, Ger.)*, 2023, **35**, 2302749.

87 L. A. Ramolise, S. N. Ogugua, H. C. Swart and D. E. Motaung, *Coord. Chem. Rev.*, 2025, **522**, 216196.

88 W. Zhang, J. Wang, L. Wang, J. Wan, G. Bai, S. Xu and L. Chen, *Adv. Opt. Mater.*, 2025, **13**, 2403290.

89 W. Zheng, M. Chen, J. Yu, F. Zhu, F. Luo, Z. Xiong and J. Guo, *Ceram. Int.*, 2025, **51**, 36233–36240.

90 R. Kiran, A. Princy, S. M. M. Kennedy, M. I. Sayyed, T. A. Hanafy, V. Mishra and S. D. Kamath, *J. Mol. Struct.*, 2025, **1322**, 140381.

91 X. Chen, J. Li, L. Chen, X. Liu, X. Jiao, Y. Peng, Y. Huang and G. Jin, *ACS Appl. Opt. Mater.*, 2025, **3**, 1410–1421.

92 L. Liu, H. Liu, W. Zou and S. Ding, *Ceram. Int.*, 2023, **49**, 28500–28505.

93 Y. Chen, J. Chen, Y. Tong, W. Zhang, X. Peng, H. Guo and D. Huang, *J. Rare Earths*, 2021, **39**, 1512–1519.

94 J. Chen, W. Zhang, S. Cui, X. Peng, F. Hu, R. Wei, H. Guo and D. Huang, *J. Alloys Compd.*, 2021, **875**, 159922.

95 J. Chen, L. Li, T. Pang, H. Guo and L. Chen, *J. Am. Ceram. Soc.*, 2023, **106**, 7514–7522.

96 Z. Cheng, M. Meng, J. Wang, Z. Li, J. He, H. Liang, X. Qiao, Y. Liu and J. Ou, *Nanoscale*, 2023, **15**, 11179–11189.

97 Y. Wang, Y. Li, C. Ma, Z. Wen, X. Yuan and Y. Cao, *J. Lumin.*, 2022, **248**, 118917.

98 X. Zhang, H. Zheng, J. Hu, F. Lu, X. Peng, R. Wei, F. Hu and H. Guo, *Ceram. Int.*, 2021, **47**, 32290–32296.

99 L. Hu, X. Lv, P. Qiao, J. Wu, D. Deng, S. Xu and H. Ma, *J. Alloys Compd.*, 2025, **1026**, 180377.

100 X. Liu, S. Shi, K. Yang, L. Chen, D. Deng and S. Xu, *J. Alloys Compd.*, 2021, **879**, 160247.

101 L. Zheng, B. Zheng, H. Xia, J. Wang, H. Song and B. Chen, *Mater. Res. Bull.*, 2021, **138**, 111210.

102 X. Zhou, S. Zhao, S. Li, Y. Wang, L. Li, S. Jiang, G. Xiang, C. Jing, J. Li and L. Yao, *J. Lumin.*, 2022, **248**, 118964.

103 B. Cao, Y. Lu, T. Zhang, H. Wu, Y. Li, C. Deng and W. Huang, *J. Mol. Struct.*, 2025, **1337**, 142193.

104 X. Ren, J. Gao, H. Shi, L. Huang, S. Zhao and S. Xu, *Optik*, 2021, **227**, 166084.

© 2025 The Author(s). Published by the Royal Society of Chemistry